

Quantitative Evaluation of Radiation-Induced Lung Injury with Hyperpolarized Xenon Magnetic Resonance

Haidong Li, Zhiying Zhang, Xiuchao Zhao, Xianping Sun, Chaohui Ye, and Xin Zhou*

Purpose: To demonstrate the feasibility of quantitative and comprehensive global evaluation of pulmonary function and microstructural changes in rats with radiation-induced lung injury (RILI) using hyperpolarized xenon MR.

Methods: Dissolved xenon spectra were dynamically acquired using a modified chemical shift saturation recovery pulse sequence in five rats with RILI (bilaterally exposed by 6-MV x-ray with a dose of 14 Gy 3 mo. prior to MR experiments) and five healthy rats. The dissolved xenon signals were quantitatively analyzed, and the pulmonary physiological parameters were extracted with the model of xenon exchange.

Results: The obtained pulmonary physiological parameters and the ratio of ^{129}Xe signal in red blood cells (RBCs) versus barrier showed a significant difference between the groups. In RILI rats versus controls, the exchange time increased from 44.5 to 112 ms, the pulmonary capillary transit time increased from 0.51 to 1.48 s, and the ratio of ^{129}Xe spectroscopic signal in RBCs versus barrier increased from 0.294 to 0.484.

Conclusion: Hyperpolarized xenon MR is effective for quantitative and comprehensive global evaluation of pulmonary function and structural changes without the use of radiation. This may open the door for its use in the diagnosis of lung diseases that are related to gas exchange. **Magn Reson Med** 76:408–416, 2016. © 2015 Wiley Periodicals, Inc.

Key words: hyperpolarized xenon; CSSR; gas exchange time; lung physiology; RILI; pulmonary function

INTRODUCTION

Thoracic cancers such as breast cancer, esophageal carcinoma, and lung cancer are a significant health concern, and pulmonary cancers are the leading causes of morbidity and mortality among malignant tumors worldwide (1,2). Radiation therapy (RT), which is widely used in the treatment of tumors, is one of the most effective therapies for treating chest tumors. Although the dose of RT is rigorously controlled to minimize its effect on normal pulmonary tissues, radiation-induced lung injury

(RILI) is still a common side effect in patients undergoing RT; more than one third of patients who receive radiotherapy develop RILI (3). RILI is usually irreversible, and it substantially reduces patient quality of life or even leads to death. The severity of RILI depends on radiation dose, lung volume and other various factors. Therefore, developing an appropriate therapy plan for each patient is one of the best ways to prevent RILI, and the noninvasive evaluation of RILI plays an important role in optimizing the RT plan (4). Usually, pulmonary function tests and imaging techniques are routine methods for the clinical diagnosis of RILI. Pulmonary function tests can detect global pulmonary function changes, but cannot comprehensively quantify physiological changes, such as air–blood exchange in the lung (5). Planar x-ray and CT are the typical imaging techniques used to assess RILI in the clinic setting, and both are able to detect the structural changes of late stage pulmonary fibrosis (6). When combined with CT, single photon emission computed tomography can also be used to evaluate pulmonary changes in patients suffering from RILI (7). However, all of these imaging modalities employ ionizing radiation, which might cause RILI patients to be exposed to a higher radiation dose when they are subjected to many scans over a short period (8). More importantly, such modalities are not able to quantify the important parameters of lung function, such as the pulmonary gas exchange time constant, capillary transit time, and total septal thickness.

In recent years, hyperpolarized noble gas NMR and MRI have been demonstrated as powerful tools to image the air space and to evaluate pulmonary gas exchange function (9–15), because the nuclear spin polarizations of hyperpolarized noble gases exceed the thermal equilibrium levels by four to five orders of magnitude via the technique of spin exchange optical pumping (SEOP) (16). Among the noble gases isotopes that are generally used in SEOP, ^3He and ^{129}Xe are the most commonly used in hyperpolarized noble gas NMR and MRI because their nuclear spin quantum number is 1/2, and they have longer longitudinal relaxation times (T_1) (17–19). Hyperpolarized ^3He MRI has been applied to detect RILI in rats and rabbits through ventilation imaging and ADC mapping (20–23). Recently, Ireland and colleagues (24–29) successfully detected RILI and optimized radiotherapy planning through hyperpolarized ^3He MRI in patients undergoing RT, but the changes in physiology and gas exchange function were not quantified.

Compared with ^3He , ^{129}Xe has unique advantages for assessing pulmonary gas exchange function and physiological changes because it has good solubility in blood

Key Laboratory of Magnetic Resonance in Biological Systems, State Key Laboratory of Magnetic Resonance and Atomic and Molecular Physics, National Center for Magnetic Resonance in Wuhan, Wuhan Institute of Physics and Mathematics, Chinese Academy of Sciences, Wuhan, 430071, P. R. China.

Grant sponsor: Natural Science Foundation of China; Grant numbers: 81227902, 11174327.

*Correspondence to: Xin Zhou, Ph.D. Professor, Wuhan Institute of Physics and Mathematics, Chinese Academy of Sciences, 30 West Xiaohongshan, Wuhan, China. E-mail: xinzhou@wipm.ac.cn

Received 19 April 2015; revised 21 July 2015; accepted 25 July 2015

DOI 10.1002/mrm.25894

Published online 24 September 2015 in Wiley Online Library (wileyonlinelibrary.com).

and tissue and possesses excellent chemical shift sensitivity to its environment (30,31). Due to these benefits, ^{129}Xe has become more attractive for biological imaging. There are two common ways to measure the gas exchange function of the lung using hyperpolarized ^{129}Xe . Xenon polarization transfer contrast (XTC), as proposed by Ruppert and colleagues (30,32), measures the decrease in the gas-phase xenon signal after saturating the dissolved xenon signals (i.e., xenon in red blood cells [RBCs] and in tissue and plasma [TP]). XTC can provide spatially resolved measurements of lung function with hyperpolarized xenon depolarization maps by taking advantage of the strong xenon signal in the gas phase. However, in XTC, the dissolved xenon signals from RBC and TP cannot be distinguished because they are treated as a single signal. Chemical shift saturation recovery (CSSR), the other method, measures the dissolved xenon signals directly (33–35). In CSSR, the xenon signals from RBC and TP are treated separately, and their dynamics as a function of the exchange time (the time between the saturation pulse and the excitation pulse) can be obtained simultaneously. CSSR has therefore proven valuable in the past to measure the dynamics of dissolved xenon signals in order to obtain the important information regarding pulmonary microstructure and function in vivo (33,35,36).

Many theoretical models have been developed to extract the quantitative parameters of lung structure and function from CSSR data. Månsson and colleagues (11,33) proposed a single exponential model that does not consider blood flow. Patz and colleagues (36,37) developed an uptake theory that considers the effect of blood flow to analyze lung function parameters. This theory was also used by Imai and colleagues (38) in a mouse model of emphysema, but the xenon signals from TP and RBC were treated as a single signal. Recently, Chang and colleagues (39,40) developed a model of xenon exchange (MOXE) based on the previous models and theories. Unlike the other two models, this model treats xenon signals from TP and RBC separately and considers the effect of blood flow. Accordingly, more physiological parameters of lung function can be quantified, including the gas exchange time constant (41,42).

In recent years, some groups have studied RILI in rats and rabbits using hyperpolarized ^{129}Xe MRI (43,44), but the comprehensive quantification of physiological changes still remains. Recently, Fox et al. (45) studied RILI with CSSR and the Månsson model in the rats and found that the exchange time constant increased at 2 wk postirradiation. However, the ratios of xenon signal in RBCs versus TP, hematocrit, pulmonary transit time, and other physiological parameters have not been quantified. More importantly, the exchange time constants $T_{\text{Tr_tissue}}$ (derived from the TP curves at 197 ppm) and $T_{\text{Tr_RBC}}$ (derived from the blood curves at 212 ppm) (33) were not found to be correlated in their study (45). We therefore proposed to address these shortcomings by using a modified CSSR and MOXE that considers the effects of perfusion more thoroughly. MOXE is a more realistic gas exchange model in which comprehensive physiological parameters can be obtained. In addition, the fitting parameters are shared and coupled, the xenon signals

from TP and RBC are fitted simultaneously, and the more reliable exchange time constant can be obtained.

In this study, hyperpolarized xenon MR spectra acquired using CSSR were used to measure pulmonary gas exchange dynamics in rats. By using MOXE, comprehensive physiological parameters were obtained to quantitatively evaluate the physiological changes in irradiated rat lungs. The physiological parameters obtained with hyperpolarized xenon MR (e.g., gas exchange time constant, pulmonary capillary transit time, septal thickness, blood hematocrit) were statistically analyzed between the RILI rats and the healthy rats.

METHODS

Hyperpolarized Xenon Gas Preparation and Delivery

Hyperpolarized ^{129}Xe gas was produced by the SEOP technique using a homebuilt polarizer that was equipped with a 75 W laser diode array of narrowed line width (QPC Lasers, Sylmar, CA) (16,46,47). The gas mixture, which comprised 1% natural abundance ^{129}Xe , 10% N_2 , and 89% ^4He , flowed through an optical cell at a rate of 0.4 standard liters per minute in the opposite direction of the laser beam. The xenon nuclear spins were polarized in the optical pumping cell, and the spin polarization of hyperpolarized xenon gas was approximately 20%. Then, hyperpolarized xenon was accumulated as ice for about an hour by flowing the gas mixture through a cold finger, which was immersed in liquid nitrogen with a magnetic field of approximately 200 mT. After hyperpolarized xenon was thawed with hot water, it was transferred to a Tedlar bag, and the available spin polarization of hyperpolarized xenon gas in the Tedlar bag was approximately 10%.

Hyperpolarized xenon gas in the Tedlar bag was connected to a homebuilt MRI-compatible hyperpolarized gas delivery system (48,49). Depending on the different experimental conditions, the rats were alternately ventilated with either oxygen or hyperpolarized xenon gas in different modes. The different ventilation modes were implemented via a National Instruments control board using a LabVIEW-based program (National Instruments, Austin, Texas, USA), which controlled pneumatic valves and solenoid valves in the gas delivery system. The delivery system could also monitor the pressure in the rat lung in real time and trigger the MRI scanner. The rats were normally ventilated with oxygen at a rate of 60 breaths per min with a tidal volume of 3 mL.

Animal Protocols

The institutional animal care committee approved all of the animal protocols. Ten Sprague-Dawley rats (180–220 g) were used in this study, and five of the rats received whole lung irradiation from a 6 MV photon x-ray (Varian Medical Systems, Palo Alto, California, USA), with a dose of 14 Gy 3 mo. before the MR experiments (50). The remaining untreated rats served as a control group. In the hyperpolarized xenon MR experiments, the rats were anesthetized with isoflurane and were alternately ventilated with either hyperpolarized xenon or oxygen through a 14-gauge catheter intubator. A combination of

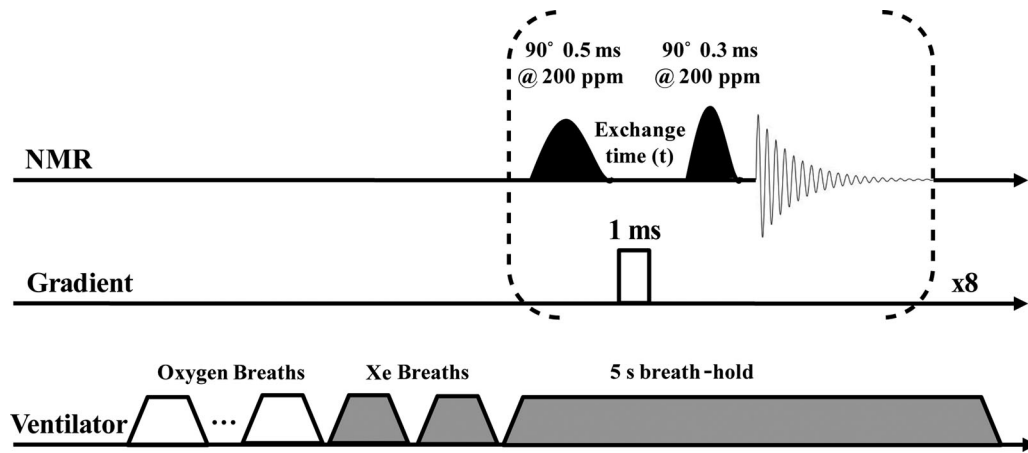


FIG. 1. Schematic of the modified chemical shift saturation recovery pulse sequence used in this study (33). Two Gaussian-shaped pulses, centered at 200 ppm relative to the gas phase (0 ppm), were applied during breath-hold after rats inhaled xenon gas for the third time. The first pulse was used to saturate the dissolved signal, and the second pulse was used to excite both gas and dissolved signals. The exchange time for xenon was varied for different acquisitions. To destroy the residual signal, a spoiler gradient was employed after the saturation pulse. Each data point was accumulated eight times to obtain better SNRs of the dissolved signals.

5% isoflurane and balanced oxygen was used to induce anesthesia in rats, and 1.5% isoflurane was used to maintain anesthesia during the surgery. After hyperpolarized xenon MR experiments, the rats were sacrificed via anesthetic overdose. The rat lungs were instilled in situ using 4% paraformaldehyde liquid at 25 cm H_2O for 30 min, after which they were extracted and immersed in 4% paraformaldehyde liquid. They were stored in 4% paraformaldehyde liquid for more than 48 h and then embedded in paraffin. The sequential sections, each with a thickness of 5 μm , were stained with hematoxylin and eosin (H&E) to assess histological changes. Alveolar septal thickness was assessed in Image-Pro Plus software (Media Cybernetics, Buckinghamshire, United Kingdom) by measuring the length of the lines drawn perpendicular to the narrowest segment of alveolar septum (51).

MR Data Acquisition

All of the experiments were conducted on a Bruker Biospec 4.7T MRI scanner with a custom-built $^{129}Xe/^1H$ dual-tuned birdcage coil (^{129}Xe at 55.4 MHz, 1H at 200.2 MHz). A modified CSSR pulse sequence was chosen to study the dynamics of hyperpolarized xenon MR signals in the lungs, as shown in Figure 1 (33). Before acquiring the CSSR data, the flip angles of RF pulses were calibrated at gas resonance (30,33), and the off-resonance effect of the excitation pulse (centered at 200 ppm) on xenon in the gas phase (0 ppm) was also measured for the dissolved xenon signal to be normalized by the actual xenon gas signal in MOXE (39). To minimally excite the alveolar xenon gas, a 90° Gaussian-shaped RF saturation pulse, which had a duration of 0.5 ms and was centered at 200 ppm, was applied to saturate the dissolved xenon signals in both TP and RBC. After a certain exchange time (t), a second 90° Gaussian-shaped RF excitation pulse, which had a duration of 0.3 ms and was centered at 200 ppm, was used to generate both dissolved phase and gas-phase xenon signals, and the dissolved phase xenon signals were normalized by the gas

xenon signal. Hyperpolarized xenon NMR data were immediately acquired after the second pulse, and the exchange time varied from 2 to 400 ms (ie, 2, 4, 6, 8, 10, 15, 20, 25, 30, 35, 40, 45, 50, 60, 70, 80, 90, 100, 150, 200, 250, 300, 350, and 400 ms). All of the MR spectra were acquired with a bandwidth of 25 KHz and 1024 sampling points. To optimize the SNRs of dissolved xenon signals, the lungs were flushed with hyperpolarized xenon gas twice. Then, xenon NMR data were acquired during the breath-hold after the rats inhaled xenon for the third time. Each data point on the recovery curves generated using the modified CSSR was accumulated eight times. The lung pressure in the rats was 12 cm H_2O in each experiment.

Data Processing

All of the spectra data were processed in the Topspin 3.0. Before the Fourier transformation, each spectrum was applied with a 50-Hz exponential line-broadening filter to reduce the noise, and Lorentzian line shapes were used to fit the three peaks (i.e., gas, TP, and RBC)

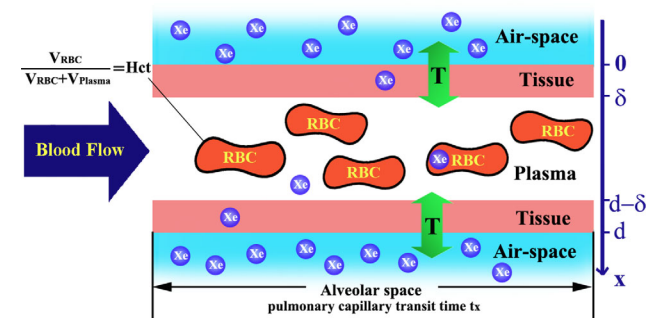


FIG. 2. Diagram of the gas exchange region of the alveoli. The total septal thickness is assumed to be d , the air-blood barrier thickness is δ . t_x is the pulmonary capillary transit time and is defined as the average time an RBC spends in the gas-exchange zone. T is the xenon gas exchange time constant in the lung. Hct is the hematocrit of the lung.

after phase correction. The peak amplitudes from the CSSR spectra at an exchange time of 100 ms were used to determine the ratio of RBCs to TP (35,42). In the calculation of the ratio of RBC/TP to gas, the amplitude of the gas signal was extracted directly from the spectra, and the flip angle applied to the xenon gas was approximately 0.6° after calibration. Then, the data were fitted to the MOXE, as shown in the following equations, to extract the physiological parameters of the lung. A schematic of the gas exchange region of the alveoli is shown in Figure 2.

$$S_{TP}(t) = b \left[\frac{2\delta}{d} - \frac{8}{\pi^2} \sum_{n=odd} \frac{1}{n^2} \left(1 - \cos\left(\frac{n\pi\delta}{d}\right) \right) e^{-n^2 t/T} \right] + b(1-\eta) \left\{ \begin{array}{l} 2 \left[\left(1 - \frac{2\delta}{d}\right) \frac{t}{t_X} - \frac{8T}{\pi^2 t_X} \sum_{n=odd} \frac{1}{n^4} \cos\left(\frac{n\pi\delta}{d}\right) (1 - e^{-n^2 t/T}) \right] \\ + \left(1 - \frac{t}{t_X}\right) \left[\left(1 - \frac{2\delta}{d}\right) - \frac{8}{\pi^2} \sum_{n=odd} \frac{1}{n^2} \cos\left(\frac{n\pi\delta}{d}\right) e^{-n^2 t/T} \right] \end{array} \right\} \quad [1]$$

$$S_{RBC}(t) = b\eta \left\{ \begin{array}{l} 2 \left[\left(1 - \frac{2\delta}{d}\right) \frac{t}{t_X} - \frac{8T}{\pi^2 t_X} \sum_{n=odd} \frac{1}{n^4} \cos\left(\frac{n\pi\delta}{d}\right) (1 - e^{-n^2 t/T}) \right] \\ + \left(1 - \frac{t}{t_X}\right) \left[\left(1 - \frac{2\delta}{d}\right) - \frac{8}{\pi^2} \sum_{n=odd} \frac{1}{n^2} \cos\left(\frac{n\pi\delta}{d}\right) e^{-n^2 t/T} \right] \end{array} \right\}, \quad [2]$$

where $S_{TP}(t)$ and $S_{RBC}(t)$ represent the normalized xenon signals in TP and RBC, respectively. The total septal wall thickness (d), the scaling factor (b) and the fraction of RBC xenon in blood (η) can be rewritten in the following manner, respectively:

$$d = \sqrt{\pi^2 D T} \quad [3]$$

$$b = \frac{\lambda d}{2} SVR \quad [4]$$

$$\eta = \frac{\lambda_{RBC}}{\lambda_p/Hct + \lambda_{RBC} - \lambda_p} \quad [5]$$

The normalized TP and RBC xenon signals ($n = 7$) were fitted to Equations [1] and [2] simultaneously using non-linear fitting in MATLAB (MathWorks, Natick, Massachusetts, USA), and the initial values for the fitting were obtained from CSSR data of a healthy rat by using an exhaustive search algorithm in Fortran (b , ranging from 0 to 0.2 with a step size of 0.0001; δ/d , ranging from 0 to 0.5 with a step size of 0.001; T , ranging from 0 to 200 ms with a step size of 0.1 ms; η , ranging from 0 to 1 with a step size of 0.001; t_X , ranging from 0 to 2 s with a step size of 0.01 s). The exchange time constant (T), the barrier-to-septum ratio (δ/d), the scaling factor (b), the fraction of RBC xenon in blood (η), and the pulmonary capillary transit time (t_X), which is defined as the average time an RBC spends in the exchange zone, can be obtained from the fitting directly. Using the diffusion coefficient for xenon in lung tissue $D \sim 3.3 \times 10^{-6} \text{ cm}^2/\text{s}$ and the average Ostwald solubility of xenon in the entire lung ($\lambda = 0.2$) (39) in the plasma ($\lambda_p = 0.09$) and in the RBC ($\lambda_{RBC} = 0.19$) (52) in Equations [3–5], the relevant physiological parameters of the lung, such as the total septal thickness (d), the blood hematocrit (Hct), the sur-

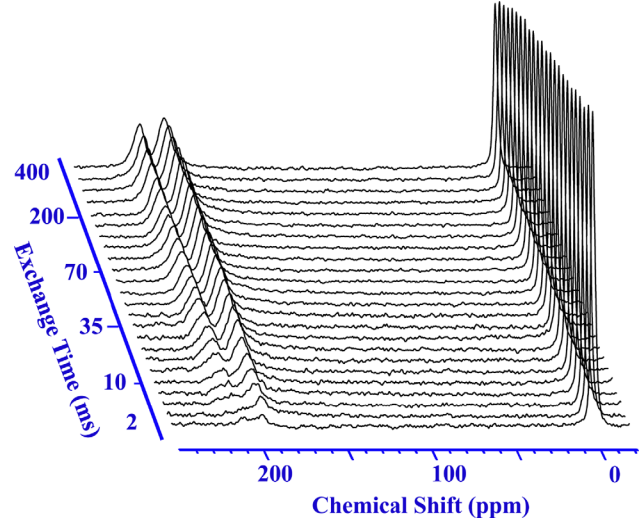


FIG. 3. The dynamics of dissolved xenon signals and gas-phase xenon signals in the healthy rat lung depending on exchange time, which varied from 2 to 400 ms.

face area to volume ratio (SVR), and the air–blood barrier thickness (δ) can be calculated.

RESULTS

Hyperpolarized Xenon Dynamics in the Lung

The dynamics of hyperpolarized xenon signals in the RBCs, TP, and airspace of healthy rat lungs depending on exchange time is shown in Figure 3. Hyperpolarized xenon signals in the RBCs, TP, and airspace could be clearly observed in all spectra, although the xenon signal in blood was small when the exchange time was short (5–20 ms), and the xenon signals in RBCs and TP increased when the exchange time increased.

Ratios of Xenon Signals in RBCs and TP

Dissolved xenon signals and gas xenon signals were obtained successfully in all healthy and RILI rats (Fig. 4). Three separate peaks could be easily distinguished and represent hyperpolarized xenon in the RBCs (212 ppm), TP (197 ppm), and airspace (0 ppm) of the lung.

There was a 1.6-fold reduction in the S_{RBC}/S_{TP} ratio in RILI rats compared with healthy rats. The mean ratios of S_{RBC}/S_{TP} in the RILI and healthy rats, which were significantly different ($P = 0.002$), were 0.294 ± 0.048 and 0.484 ± 0.078 , respectively (Fig. 5). The S_{TP}/S_{Gas} ratio in the RILI rats increased significantly ($P = 0.002$) compared with the healthy rats. The mean S_{TP}/S_{Gas} ratio in the RILI rats was 0.341 ± 0.048 compared with 0.243 ± 0.013 in the healthy rats, which was a 1.4-fold difference (Fig. 5). All of the ratios are summarized in Table 1.

Analysis of the Parameters Using MOXE

The TP and RBC xenon signals, which were normalized by the corresponding gas signal, were plotted against the exchange time and then fitted to Equations [1] and [2] simultaneously, as shown in Figure 6. There was an increase in xenon signal in the tissue and plasma of the

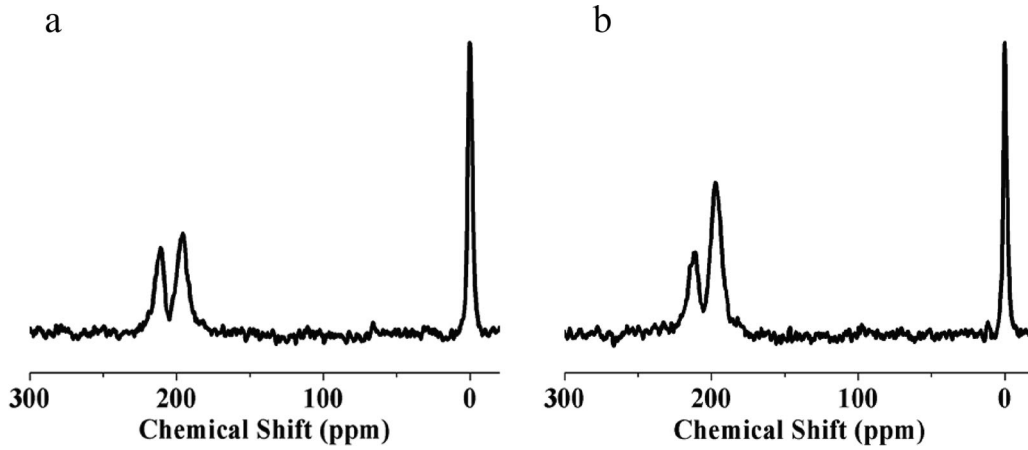


FIG. 4. Typical xenon spectra with 50 Hz line-broadening in a healthy rat (a) and in a RILI rat (b). In the RILI rat, the xenon signal in the TP (197 ppm) increased compared with the healthy rat, whereas the xenon signal in the RBCs (212 ppm) was similar to the healthy rat. The spectra were acquired with an exchange time of 100 ms.

RILI rats compared with the healthy rats; however, there was no significant difference in the signal in RBCs between the groups.

The comprehensive physiological parameters of the lung were calculated using MOXE. The mean exchange time constant (T) and pulmonary capillary transit time (t_X) were 44.5 ± 7.9 ms and 0.51 ± 0.15 s, respectively, in the healthy rats and 112.0 ± 9.5 ms and 1.48 ± 0.52 s, respectively, in the RILI rats. T and t_X were significantly different between the RILI and the healthy rats ($P < 0.005$). The fraction of RBC xenon in blood (η) was also significantly different ($P = 0.009$) between the RILI and the healthy rats; the mean fraction of RBC xenon in blood was 0.44 ± 0.07 in the healthy rats and 0.31 ± 0.05 in the RILI rats. Significant differences were also found between the healthy and RILI rats in the total septal thickness (d) and blood hematocrit (Hct). The comprehensive parameters are summarized in Table 2, along with the P values denoting statistical significance.

Histopathological Observations in H&E-Stained Lung Tissue

As shown in Figure 7, interstitial alveolar wall thickening and the accumulation of inflammatory cell infiltration were observed in the entire lung among the RILI rats, and collagen deposition was also found in the lungs

of the RILI rats. The septal thickness in the RILI rats increased considerably compared with controls ($P < 0.001$), and the mean septal thickness was 8.4 ± 1.3 μm and 5.7 ± 0.3 μm , respectively, in the RILI rats and healthy rats.

DISCUSSION

There was a significant difference in the $S_{\text{RBC}}/S_{\text{TP}}$ ratio between the RILI rats and healthy rats. The $S_{\text{RBC}}/S_{\text{TP}}$ ratio in the RILI rats (0.294 ± 0.058) decreased by approximately 40% compared with that in the healthy rats (0.484 ± 0.078). A similar reduction, but one that occurred for different reasons, was observed in a previous study in patients who had idiopathic pulmonary fibrosis (53). In these patients, the reduction in the $S_{\text{RBC}}/S_{\text{TP}}$ ratio resulted from an approximately two-fold decrease in the $S_{\text{RBC}}/S_{\text{Gas}}$ ratio and an approximately 1.6-fold increase in the $S_{\text{TP}}/S_{\text{Gas}}$ ratio compared with healthy subjects (53). However, in the present study, the change in the $S_{\text{RBC}}/S_{\text{TP}}$ ratio was caused primarily by xenon signal in the TP. In addition, the $S_{\text{TP}}/S_{\text{Gas}}$ ratio in the RILI rats (0.341 ± 0.048) increased by approximately 1.4-fold compared with that in the healthy rats (0.243 ± 0.013). This occurred largely because the RILI rats used in this study were approximately 3 mo. post-radiation treatment, which is in the first phase of the RILI disease

Table 1
 $S_{\text{RBC}}/S_{\text{Gas}}$, $S_{\text{TP}}/S_{\text{Gas}}$, and $S_{\text{RBC}}/S_{\text{TP}}$ Ratios in Healthy and RILI Rats

	Healthy Rats			RILI Rats		
	$S_{\text{RBC}}/S_{\text{Gas}}$	$S_{\text{TP}}/S_{\text{Gas}}$	$S_{\text{RBC}}/S_{\text{TP}}$	$S_{\text{RBC}}/S_{\text{Gas}}$	$S_{\text{TP}}/S_{\text{Gas}}$	$S_{\text{RBC}}/S_{\text{TP}}$
Rat 1	0.117	0.254	0.461	0.077	0.311	0.247
Rat 2	0.133	0.230	0.577	0.141	0.371	0.379
Rat 3	0.120	0.238	0.504	0.121	0.401	0.302
Rat 4	0.095	0.259	0.366	0.087	0.281	0.310
Rat 5	0.119	0.232	0.512	0.079	0.342	0.232
Mean \pm SD	0.117 ± 0.014	0.243 ± 0.013	0.484 ± 0.078	0.101 ± 0.029	0.341 ± 0.048	0.294 ± 0.058

The amplitude of the gas signal was extracted directly from spectra (at an exchange time of 100 ms) when the $S_{\text{RBC}}/S_{\text{Gas}}$ and $S_{\text{TP}}/S_{\text{Gas}}$ ratios were calculated, and the flip angle applied to the xenon gas was approximately 0.6° .

Abbreviation: SD, standard deviation.

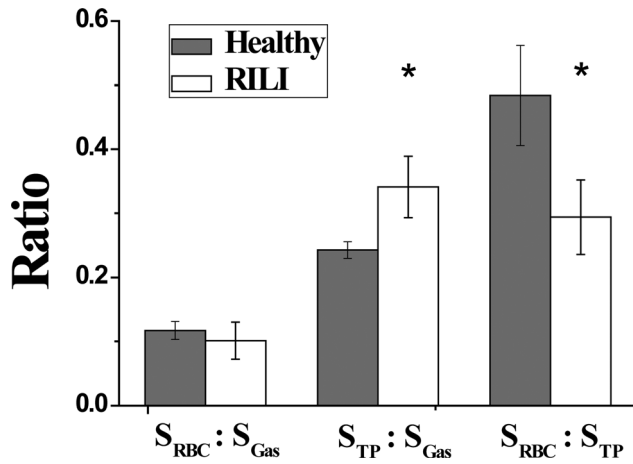


FIG. 5. Comparison of the S_{RBC}/S_{Gas} , S_{TP}/S_{Gas} , and S_{RBC}/S_{TP} ratios between the healthy and the RILI rats. Compared with the healthy rats, the S_{RBC}/S_{TP} ratio in the RILI rats diminished significantly ($P = 0.002$), and there was a significant 1.4-fold increase in the mean S_{TP}/S_{Gas} ratio in the RILI rats ($P = 0.002$). However, there was no significant difference between the RILI and healthy rats in the S_{RBC}/S_{Gas} ratio.

process, when radiation pneumonitis occurs (Fig. 7) (54,55). The pulmonary septum in the RILI rats became thicker than that in the healthy rats. In addition, more xenon dissolved in the barrier of the RILI rats, and the S_{TP}/S_{Gas} ratio increased. However, there was no signifi-

cant difference in the S_{RBC}/S_{Gas} ratio ($P = 0.309$) between the healthy (0.117 ± 0.014) and RILI (0.101 ± 0.029) rats, which indicates that there was almost no change in the amount of RBCs in the exchange zone 3 mo. after radiation treatment, because the RBC signal only came from dissolved xenon in the RBC.

The mean exchange time constant (T) increased significantly in the RILI rats compared with the healthy rats because the thicker septum of the irradiated rats resulted in greater hyperpolarized xenon diffusion from the airspace in the alveoli into the capillaries in the RILI rats compared with the healthy rats. Additionally, the time to S_{TP} and S_{RBC} saturation was longer. The exchange time constant (T) that was obtained from the healthy rats in this study is in agreement with the results found by using CSSR (33,45). A longer exchange time was also reported in a recent study that used the Månsson exchange model to explore hyperpolarized xenon spectra in RILI rats two weeks after radiation treatment (45). A significant increase in the pulmonary capillary transit time (t_x) was also observed in RILI rats. This was due to the widespread obstruction caused by platelets, collagen, and fibrin, which occurred in the capillaries of the RILI rats 3 mo. after radiation and resulted in both a decrease in blood flow (56,57) and an increase in the average time that the RBCs spent in the exchange zone. Previous studies on healthy rats that used non-NMR methods have reported a total pulmonary blood flow of 2 mL/s (58) and a total capillary volume of approximately 1 mL (59).

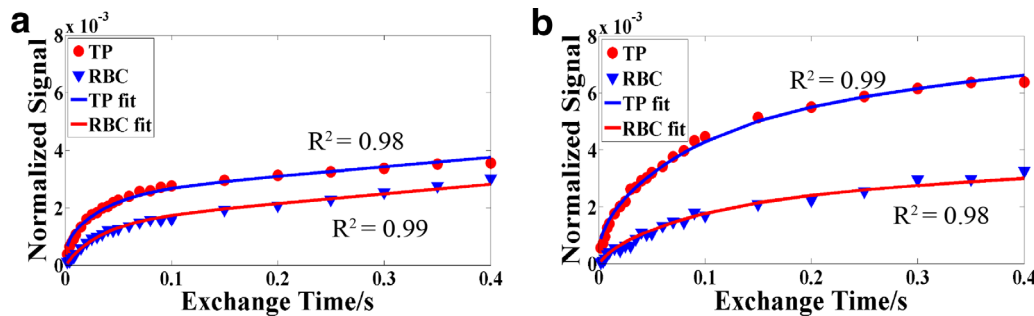


FIG. 6. Typical recovery signals (circles and triangles) and fittings (lines) of the dissolved xenon in the TP and RBCs as a function of exchange time (i.e., the delay between the pulses in the CSSR sequence) in a healthy rat (a) and a RILI rat (b). The signal in the TP in the healthy rat is considerably smaller than that in the RILI rat.

Table 2
Comprehensive Physiological Parameters of the Lung Calculated Using MOXE

Parameter	Symbol	Healthy Rats	RILI Rats	P
Scaling factor	b	0.0044 ± 0.0003	0.0077 ± 0.0010	0.001
Barrier-to-septum ratio	δ/d	0.104 ± 0.059	0.064 ± 0.027	0.216
Exchange time constant	T (ms)	44.5 ± 7.9	112.0 ± 9.5	<0.001
Fraction RBC xenon in blood	η	0.442 ± 0.071	0.307 ± 0.052	0.009
Pulmonary capillary transit time	t_x (s)	0.508 ± 0.151	1.475 ± 0.518	0.004
Septal wall thickness	d (μm)	12.0 ± 1.1	19.1 ± 0.8	<0.001
Thickness of air-blood barrier	δ (μm)	1.24 ± 0.73	1.23 ± 0.56	0.985
Surface area to volume ratio	SVR (cm^{-1})	37.1 ± 1.7	40.3 ± 6.4	0.336
Blood hematocrit	Hct	0.277 ± 0.057	0.176 ± 0.036	0.010

Values are shown as the mean \pm standard deviation; standard deviations were based solely on the variations among different animals within each group.

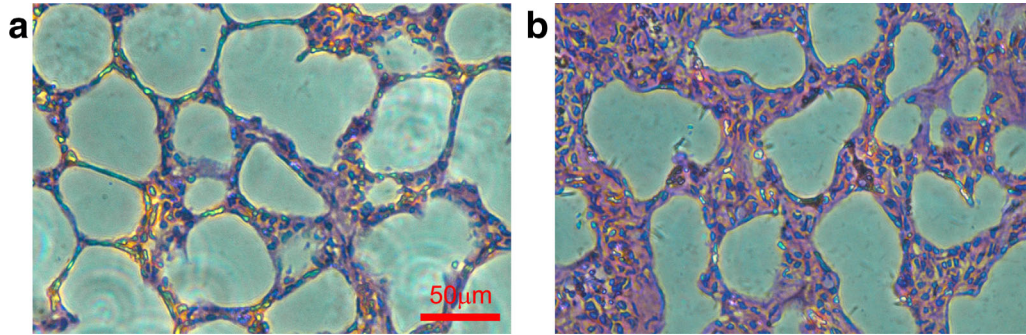


FIG. 7. Typical H&E-stained lung images of a healthy (a) and a RILI rat (b). In the RILI rat, the alveolar wall was considerably thicker, and there was an accumulation of inflammatory cell infiltration. Magnification = 40 \times .

From these data, the pulmonary capillary transit time is calculated to be 0.5 s, which is in agreement with the value (0.51 ± 0.15 s) measured in the healthy rats in our study.

There was a significant difference in the mean septal thickness measured using MOXE between the RILI and healthy rats. In the healthy rats, the total septal thickness was approximately 12.0 ± 1.1 μm , which is in agreement with the findings of a previous study (33). The total septal thickness was 19.1 ± 0.8 μm in the RILI rats and approximately 1.5-fold larger than that in the healthy rats. The increase in the septal thickness of the RILI rats was significant and was due to the accumulation of inflammatory cell infiltration and the thickening of the alveolar wall after the rats were treated with x-ray radiation, which is clearly visible in Figure 7. The increase of septal thickness in RILI rats measured using hyperpolarized xenon MR was also confirmed by the quantitative measurement using images of histology (5.7–8.4 μm). Additionally, the septal thickness measured using histology and MOXE are well correlated ($R^2 = 0.82$), as shown in Figure 8. The septal thickness measured in the histology was smaller compared with that derived from

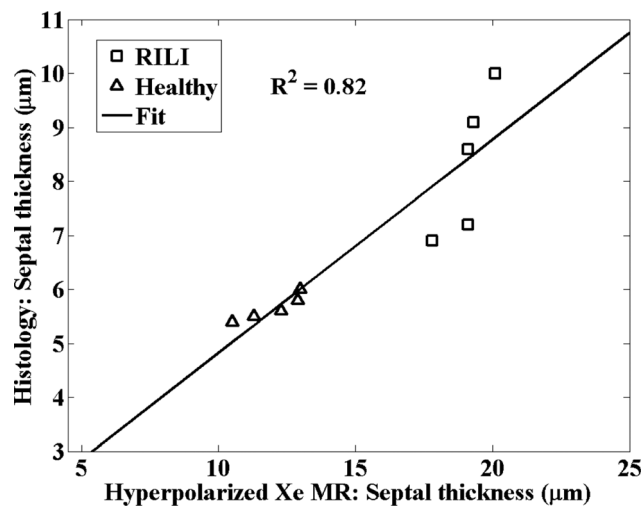


FIG. 8. Correlation of septal thickness measured using histology and hyperpolarized Xe MR. The solid line is a linear, least squares fit of the data and indicates that the septal thickness measured using the two methods correlated well ($R^2 = 0.82$).

MOXE, because the narrowest segment of alveolar septum was used for measurement in histology analysis.

The value of *Hct* (0.176 ± 0.036) in the RILI rats that was measured in this study was significantly lower ($P = 0.01$) than that in the healthy rats (0.277 ± 0.057), and the *Hct* measured in this study was lower than that reported in the previous study (~ 0.4) (60). This was most likely because xenon signals from plasma and the air–blood barrier have the same chemical shift (197 ppm) and cannot be distinguished in the CSSR spectra. As a consequence, fitting to xenon gas exchange models (i.e., MOXE and the Månsson model) can result in an overestimation of the xenon plasma signal, which, in turn, is reflected in a decrease of the fitted *Hct* value. Previous studies also found that the fitted *Hct* parameter values were lower than those from blood samples and that the *Hct* values in patients with pulmonary fibrosis were reduced compared with those in healthy volunteers (42).

The mean air–blood barrier thickness measured in the healthy rats was 1.24 ± 0.73 μm , which is in agreement with the value of 1.25 μm that was reported in a previous study (61,62). The mean air–blood barrier thickness did not show a significant difference ($P = 0.985$) between the healthy rats (1.24 ± 0.73 μm) and the RILI rats (1.23 ± 0.56 μm). However, the air–blood barrier of the RILI rats was noticeably thicker than that of the healthy rats (Fig. 7). The inconsistency in the results observed is primarily due to the limitation of the fitting model that was mentioned previously (i.e., the xenon signal from tissue and plasma could not be distinguished in the MOXE).

Although the mean *SVR* was slightly smaller in the healthy rats than in the RILI rats, there was no significant difference ($P = 0.336$) in the *SVR* between the groups in this study. The measured mean *SVR* was 37.1 ± 1.7 cm^{-1} and 40.3 ± 6.4 cm^{-1} in the healthy and RILI rats, respectively. Based on the histopathological images of the lung tissues, the lung septum of the RILI rats increased compared with that of the healthy rats. This caused the size of the alveoli to decrease in the RILI rats (56), which led to an increase in the *SVR*. However, the change in alveolar size did not significantly affect alveolar *SVR*, and there were no significant changes when considering the individual differences.

A previous study has shown that the parameters extracted using MOXE are significantly correlated with

those extracted using existing models (i.e., the Månsson and Patz models) ($P < 0.01$) (42). MOXE is a complex model for fitting in which five parameters are shared between $S_{TP}(t)$ and $S_{RBC}(t)$. Thus, these two expressions are completely correlated, and the data from TP and RBCs should be fitted to the two expressions simultaneously to obtain accurate results. As demonstrated in a previous study, constraining the fit parameters benefits the fitting results, and the restricted parameter has a negligible effect on the other fitting parameters (42). In our study, the same set of initial values was used for all fittings, and no unrealistic parameters were observed.

CONCLUSION

In this study, we comprehensively quantified physiological parameters to evaluate pulmonary function and microstructure by using hyperpolarized xenon MR spectra. By using the MOXE, a more reliable and accurate exchange time constant was obtained, and it was found to be significantly increased in RILI rats in comparison with healthy rats. Additionally, to the best of our knowledge, the majority of physiological parameters in the RILI rats, including pulmonary capillary transit time, septal thickness and S_{RBC}/S_{TP} ratio, were comprehensively and quantitatively analyzed, and they were significantly different from those in the control rats. These results demonstrate that hyperpolarized xenon MR is a powerful tool for noninvasively quantifying the parameters of pulmonary function and structure, particularly in pulmonary diseases that are related to gas exchange.

REFERENCES

1. Årnlöv J, Larsson A. Global, regional, and national age–sex specific all-cause and cause-specific mortality for 240 causes of death, 1990–2013: a systematic analysis for the Global Burden of Disease Study 2013. *Lancet* 2014;385:117–171.
2. Ferlay J, Shin HR, Bray F, Forman D, Mathers C, Parkin DM. Estimates of worldwide burden of cancer in 2008: GLOBOCAN 2008. *Int J Cancer* 2010;127:2893–2917.
3. Mehta V. Radiation pneumonitis and pulmonary fibrosis in non-small-cell lung cancer: pulmonary function, prediction, and prevention. *Int J Radiat Oncol Biol Phys* 2005;63:5–24.
4. Pereira GC, Traugher M, Muzic RF Jr. The role of imaging in radiation therapy planning: past, present, and future. *Biomed Res Int* 2014;2014:231090.
5. Guckenberger M, Klement RJ, Kestin LL, et al. Lack of a dose-effect relationship for pulmonary function changes after stereotactic body radiation therapy for early-stage non-small cell lung cancer. *Int J Radiat Oncol Biol Phys* 2013;85:1074–1081.
6. Ikezoe J, Takashima S, Morimoto S, Kadowaki K, Takeuchi N, Yamamoto T, Nakanishi K, Isaza M, Arisawa J, Ikeda H. CT appearance of acute radiation-induced injury in the lung. *AJR Am J Roentgenol* 1988;150:765–770.
7. Zhang W, Wang J, Tang M, Pan J, Bai P, Lin D, Qian F, Lin F, Yang X, Zhang S. Quantitative study of lung perfusion SPECT scanning and pulmonary function testing for early radiation-induced lung injury in patients with locally advanced non-small cell lung cancer. *Exp Ther Med* 2012;3:631–635.
8. Davis SD, Yankelevitz DF, Henschke CI. Radiation effects on the lung: clinical features, pathology, and imaging findings. *Am J Roentgenol* 1992;159:1157–1164.
9. Albert MS, Cates GD, Driehuys B, Happer W, Saam B, Springer CS, Wishnia A. Biological magnetic resonance imaging using laser-polarized Xe-129. *Nature* 1994;370:199–201.
10. Driehuys B, Walker J, Pollaro J, Cofer GP, Mistry N, Schwartz D, Johnson GA. He-3 MRI in mouse models of asthma. *Magn Reson Med* 2007;58:893–900.
11. Driehuys B, Cofer GP, Pollaro J, Mackel JB, Hedlund LW, Johnson GA. Imaging alveolar-capillary gas transfer using hyperpolarized Xe-129 MRI. *Proc Natl Acad Sci U S A* 2006;103:18278–18283.
12. Dregely I, Mugler JP III, Ruset IC, et al. Hyperpolarized xenon-129 gas-exchange imaging of lung microstructure: first case studies in subjects with obstructive lung disease. *J Magn Reson Imaging* 2011;33:1052–1062.
13. Marshall H, Parra-Robles J, Deppe MH, Lipson DA, Lawson R, Wild JM. ^3He pO₂ mapping is limited by delayed-ventilation and diffusion in chronic obstructive pulmonary disease. *Magn Reson Med* 2014;71:1172–1178.
14. Six JS, Hughes-Riley T, Lilburn DM, Dorkes AC, Stupic KF, Shaw DE, Morris PG, Hall IP, Pavlovskaya GE, Meersmann T. Pulmonary MRI contrast using surface quadrupolar relaxation (SQUARE) of hyperpolarized ^{83}Kr . *Magn Reson Imaging* 2014;32:48–53.
15. Mugler JP, Altes TA, Ruset IC, Dregely IM, Mata JF, Miller GW, Ketel S, Ketel J, Hersman FW, Ruppert K. Simultaneous magnetic resonance imaging of ventilation distribution and gas uptake in the human lung using hyperpolarized xenon-129. *Proc Natl Acad Sci U S A* 2010;107:21707–21712.
16. Walker TG, Happer W. Spin-exchange optical pumping of noble-gas nuclei. *Rev Mod Phys* 1997;69:629–642.
17. Nikolaou P, Coffey AM, Walkup LL, et al. Near-unity nuclear polarization with an open-source ^{129}Xe hyperpolarizer for NMR and MRI. *Proc Natl Acad Sci USA* 2013;110:14150–14155.
18. Zhou X, Graziani D, Pines A. Hyperpolarized xenon NMR and MRI signal amplification by gas extraction. *Proc Natl Acad Sci U S A* 2009;106:16903–16906.
19. Chawla MS, Chen XJ, Möller HE, Cofer GP, Wheeler CT, Hedlund LW, Johnson GA. In vivo magnetic resonance vascular imaging using laser-polarized ^3He microbubbles. *Proc Natl Acad Sci U S A* 1998;95:10832–10835.
20. Yablonskiy DA, Sukstanskii AL, Leawoods JC, Gierada DS, Bretthorst GL, Lefrak SS, Cooper JD, Conradi MS. Quantitative in vivo assessment of lung microstructure at the alveolar level with hyperpolarized ^3He diffusion MRI. *Proc Natl Acad Sci U S A* 2002;99:3111–3116.
21. Chen XJ, Hedlund LW, Möller HE, Chawla MS, Hannon RR, Johnson GA. Detection of emphysema in rat lungs by using magnetic resonance measurements of ^3He diffusion. *Proc Natl Acad Sci U S A* 2000;97:11478–11481.
22. Ward ER, Hedlund LW, Kurylo WC, Wheeler CT, Cofer GP, Dewhurst MW, Marks LB, Vujaskovic Z. Proton and hyperpolarized helium magnetic resonance imaging of radiation-induced lung injury in rats. *Int J Radiat Oncol Biol Phys* 2004;58:1562–1569.
23. Cai J, Mata JF, Orton MD, Hagspiel KD, Mugler JP, Larner JM, Sheng K, Read PW. A rabbit irradiation platform for outcome assessment of lung stereotactic radiosurgery. *Int J Radiat Oncol Biol Phys* 2009;73:1588–1595.
24. Ireland RH, Bragg CM, McJury M, Woodhouse N, Fischele S, Van Beek EJ, Wild JM, Hatton MQ. Feasibility of image registration and intensity-modulated radiotherapy planning with hyperpolarized helium-3 magnetic resonance imaging for non-small-cell lung cancer. *Int J Radiat Oncol Biol Phys* 2007;68:273–281.
25. Ireland RH, Din OS, Swinscoe JA, Woodhouse N, van Beek EJ, Wild JM, Hatton MQ. Detection of radiation-induced lung injury in non-small cell lung cancer patients using hyperpolarized helium-3 magnetic resonance imaging. *Radiation Oncol* 2010;97:244–248.
26. Bates EL, Bragg CM, Wild JM, Hatton MQ, Ireland RH. Functional image-based radiotherapy planning for non-small cell lung cancer: a simulation study. *Radiation Oncol* 2009;93:32–36.
27. Hodge C, Tomé WA, Fain S, Bentzen S, Mehta M. On the use of hyperpolarized helium MRI for conformal avoidance lung radiotherapy. *Med Dosim* 2011;35:297–303.
28. Hoover DA, Capaldi DP, Sheikh K, Palma DA, Rodrigues GB, Dar AR, Yu E, Dingle B, Landis M, Kocha W. Functional lung avoidance for individualized radiotherapy (FLAIR): study protocol for a randomized, double-blind clinical trial. *BMC Cancer* 2014;14:934.
29. Cai J, McLawhorn R, Altes TA, de Lange E, Read PW, Larner JM, Benedict SH, Sheng K. Helical tomotherapy planning for lung cancer based on ventilation magnetic resonance imaging. *Med Dosim* 2012;36:389–396.
30. Ruppert K, Brookeman JR, Hagspiel KD, Mugler JP. Probing lung physiology with xenon polarization transfer contrast (XTC). *Magn Reson Med* 2000;44:349–357.

31. Miller KW, Reo NV, Uiterkamp AS, Stengle DP, Stengle TR, Williamson KL. Xenon NMR: chemical shifts of a general anesthetic in common solvents, proteins, and membranes. *Proc Natl Acad Sci U S A* 1981;78:4946–4949.
32. Ruppert K, Mata JF, Brookeman JR, Hagspiel KD, Mugler JP. Exploring lung function with hyperpolarized Xe-129 nuclear magnetic resonance. *Magn Reson Med* 2004;51:676–687.
33. Månsson S, Wolber J, Driehuys B, Wollmer P, Golman K. Characterization of diffusing capacity and perfusion of the rat lung in a lipopolysaccharide disease model using hyperpolarized Xe-129. *Magn Reson Med* 2003;50:1170–1179.
34. Sakai K, Bilek AM, Oteiza E, Walsworth RL, Balamore D, Jolesz FA, Albert MS. Temporal dynamics of hyperpolarized ^{129}Xe resonances in living rats. *J Magn Reson B* 1996;111:300–304.
35. Qing K, Mugler JP, Altes TA, Jiang Y, Mata JF, Miller GW, Ruset IC, Hersman FW, Ruppert K. Assessment of lung function in asthma and COPD using hyperpolarized ^{129}Xe chemical shift saturation recovery spectroscopy and dissolved-phase MRI. *NMR Biomed* 2014;27:1490–1501.
36. Patz S, Muradyan I, Hrovat MI, Dabaghyan M, Washko GR, Hatabu H, Butler JP. Diffusion of hyperpolarized Xe-129 in the lung: a simplified model of Xe-129 septal uptake and experimental results. *New J Phys* 2011;13:015009.
37. Patz S BJ, Muradyan I, Hrovat MI, Hatabu H, Dellaripa PF, Dregely IM, Ruset I, Hersman FW. Detection of Interstitial Lung Disease in Humans with Hyperpolarized ^{129}Xe . In Proceedings of the 16th Annual Meeting of ISMRM, Toronto, Ontario, Canada, 2008. Abstract 2678.
38. Imai H, Kimura A, Iguchi S, Hori Y, Masuda S, Fujiwara H. Noninvasive detection of pulmonary tissue destruction in a mouse model of emphysema using hyperpolarized ^{129}Xe MRS under spontaneous respiration. *Magn Reson Med* 2010;64:929–938.
39. Chang YV. MOXE: a model of gas exchange for hyperpolarized ^{129}Xe magnetic resonance of the lung. *Magn Reson Med* 2013;69:884–890.
40. Chang YV, Quirk JD, Ruset IC, Atkinson JJ, Hersman FW, Woods JC. Quantification of human lung structure and physiology using hyperpolarized Xe-129. *Magn Reson Med* 2014;71:339–344.
41. Freeman MS, Cleveland ZI, Qi Y, Driehuys B. Enabling hyperpolarized Xe-129 MR spectroscopy and imaging of pulmonary gas transfer to the red blood cells in transgenic mice expressing human hemoglobin. *Magn Reson Med* 2013;70:1192–1199.
42. Stewart NJ, Leung G, Norquay G, et al. Experimental validation of the hyperpolarized ^{129}Xe chemical shift saturation recovery technique in healthy volunteers and subjects with interstitial lung disease. *Magn Reson Med* 2015;74:196–207.
43. Driehuys B, Raidy T, Pollaro J, Johnson A, Dewhirst M, Marks L, Vujaskovic Z. Hyperpolarized ^{129}Xe MRI for functional assessment of radiation-induced lung injury. *Int J Radiat Oncol Biol Phys* 2005;63:S460–S461.
44. Ruppert K, Mata JF, Cai J, et al. Detecting Radiation-Induced Lung Injuries Using XTC MRI: Initial Findings. In Proceedings of the 15th Annual Meeting of ISMRM, Berlin, Germany, 2007. Abstract 456.
45. Fox MS, Ouriadov A, Thind K, Hegarty E, Wong E, Hope A, Santyr GE. Detection of radiation induced lung injury in rats using dynamic hyperpolarized Xe-129 magnetic resonance spectroscopy. *Med Phys* 2014;41:072302.
46. Zhou X. Hyperpolarized noble gases as contrast agents. In: Schröder L, Faber C, editors. *In vivo NMR imaging*. New York, NY: Humana Press; 2011. p 189–204.
47. Zhou X, Luo J, Sun X, Zeng X, Ding S, Liu M, Zhan M. Enhancement of solid-state proton NMR via the spin-polarization-induced nuclear Overhauser effect with laser-polarized xenon. *Phys Rev B* 2004;70:052405.
48. Nouls J, Fanarjian M, Hedlund L, Driehuys B. A constant-volume ventilator and gas recapture system for hyperpolarized gas MRI of mouse and rat lungs. *Concept Magn Reson B* 2011;39B:78–88.
49. Hedlund LW, Cofer GP, Owen SJ, Johnson GA. MR-compatible ventilator for small animals: computer-controlled ventilation for proton and noble gas imaging. *Magn Reson Imaging* 2000;18:753–759.
50. Thind K, Chen A, Friesen-Waldner L, Ouriadov A, Scholl TJ, Fox M, Wong E, VanDyk J, Hope A, Santyr G. Detection of radiation-induced lung injury using hyperpolarized ^{13}C magnetic resonance spectroscopy and imaging. *Magn Reson Med* 2013;70:601–609.
51. He M, Cheng N, Gao W-w, Zhang M, Zhang Y-y, Richard DY, Wang M-w. Characterization of Quin-C1 for its anti-inflammatory property in a mouse model of bleomycin-induced lung injury. *Acta Pharmacol Sin* 2011;32:601–610.
52. Ladefoge J, Andersen AM. Solubility of xenon-133 at 37°C in water, saline, olive oil, liquid paraffin, solutions of albumin, and blood. *Phys Med Biol* 1967;12:353–358.
53. Kaushik SS, Freeman MS, Yoon SW, Liljereth MG, Stiles JV, Roos JE, Foster WM, Rackley CR, McAdams HP, Driehuys B. Measuring diffusion-limitation with a perfusion-limited gas-hyperpolarized ^{129}Xe gas-transfer spectroscopy in patients with idiopathic pulmonary fibrosis. *J Appl Physiol* 2014;117:577–585.
54. Ding K, Bayouth JE, Buatti JM, Christensen GE, Reinhardt JM. 4D CT-based measurement of changes in pulmonary function following a course of radiation therapy. *Med Phys* 2010;37:1261–1272.
55. Ghafoori P, Marks LB, Vujaskovic Z, Kelsey CR. Radiation-induced lung injury—assessment, management, and prevention. *Oncology (Williston Park)* 2008;22:37–47.
56. Gross NJ. Pulmonary effects of radiation-therapy. *Ann Intern Med* 1977;86:81–92.
57. Gross N. The pathogenesis of radiation-induced lung damage. *Lung* 1981;159:115–125.
58. Müller B, Mannesmann G. Measurement of cardiac output by the thermodilution method in rats. II. Simultaneous measurement of cardiac output and blood pressure in conscious rats. *J Pharmacol Methods* 1981;5:29–34.
59. Altman PL, Dittmer DS. *Respiration and circulation*. Bethesda, MD: Federation of American Societies for Experimental Biology; 1971. 930 p.
60. Probst RJ, Lim JM, Bird DN, Pole GL, Sato AK, Claybaugh JR. Gender differences in the blood volume of conscious Sprague-Dawley rats. *J Am Assoc Lab Anim Sci* 2006;45:49–52.
61. Weibel ER, Knight BW. A morphometric study on the thickness of the pulmonary air-blood barrier. *J Cell Biol* 1964;21:367–384.
62. Mercer RR, Russell ML, Crapo JD. Alveolar septal structure in different species. *J Appl Physiol* 1994;77:1060–1066.